



# Near-interface flow modeling in large-eddy simulation of two-phase turbulence

Lluís Jofre<sup>a,b,\*</sup>, Michael S. Dodd<sup>a</sup>, Joan Grau<sup>b</sup>, Ricardo Torres<sup>b</sup>

<sup>a</sup> Center for Turbulence Research, Stanford University, Stanford, CA 94305, USA

<sup>b</sup> Department of Fluid Mechanics, Technical University of Catalonia – BarcelonaTech, Barcelona 08019, Spain

## ARTICLE INFO

### Article history:

Received 12 May 2020

Revised 24 June 2020

Accepted 2 July 2020

Available online 6 August 2020

### Keywords:

Large-Eddy simulation

Near-interface flow modeling

Turbulence

Two-phase flow

## ABSTRACT

The smallest hydrodynamic length scales in two-phase turbulence are located at the interface between phases, or fluids, as a result of two-way coupling phenomena. Typically, these interface-generated scales are several times smaller than the dissipative scales in the surrounding bulk flow identified by Kolmogorov's 1941 theory. Consequently, to properly capture these interface-generated small scales with sufficiently fine resolutions, the computational cost of performing large-eddy simulations of two-phase turbulent flow increases significantly from its (single-phase) theoretical optimum and toward values on the order of the direct numerical simulation of turbulence. Therefore, to maintain the cost of scale-resolving approaches linear with respect to the Reynolds number, this work investigates the modeling of the small-scale fluid motions in the vicinity of the viscous near-interface region of two-phase turbulent flows. Given the resemblance between the flow structures in the near-interface regions and those found in the boundary layers of turbulent wall-bounded flow, the modeling methodology proposed is inspired by ideas developed for turbulent flows interacting with solid walls, but modified to capture slip-velocity effects between phases. The performance of the approach is *a priori* assessed by utilizing data from direct numerical simulations of decaying isotropic turbulence laden with droplets of super-Kolmogorov size, demonstrating its computational feasibility and potential for reducing the cost of large-eddy simulation studies of two-phase turbulence.

© 2020 Elsevier Ltd. All rights reserved.

## 1. Introduction

The interaction of turbulence with two-phase interfaces encompasses very complex multiscale flow phenomena of interest in a wide range of engineering and scientific applications, like for example rain formation in clouds (Grabowski and Wang, 2013), spray atomization in combustors (Sirignano, 1983; Faeth et al., 1995; Jofre and Urzay, 2020), and microbubble generation in biomedical and processing technologies (Rodríguez-Rodríguez et al., 2015). In such systems, the dispersed phase typically undergoes significant rates of deformation and break-up/coalescence events due to vortical and straining flow motions, and/or external forces, that greatly increase the surface area between phases. In these near-interface regions, turbulence is modulated as a result of two-way coupling effects (Dodd and Ferrante, 2016), favoring low-enstrophy/high-dissipation motions with characteristic sizes significantly smaller

than the dissipative scales in the bulk of the carrier phase (Dodd and Jofre, 2018; 2019).

The inherent nonlinearity of the flow mechanisms encountered, together with the numerous challenges associated with performing experiments, renders computational approaches an indispensable tool for the analysis, design and optimization of two-phase turbulence phenomena in industrial and natural problems. In this regard, direct numerical simulation (DNS) of turbulent two-phase flows (Elghobashi, 2019), resolving all length and time scales of turbulence interacting with interfaces, is now feasible for moderate Reynolds numbers or for reduced computational complexity, viz. interfaces undergoing small deformation and/or limited number of droplets/bubbles. Selected examples of DNS studies in the past decade include mixing layers and free-surface problems (Agbaglah et al., 2017; Almagro et al., 2017; Ling et al., 2019; Deike et al., 2016), bubbly flows (Balcázar et al., 2015; Lin et al., 2018; Chan et al., 2019), sprays and atomization processes (Gorokhovski and Herrmann, 2008; Shinjo and Umemura, 2010; Desjardins and Pitsch, 2010), and multiphysics flows (Prosperetti, 2017; Lu et al., 2017; Rasthofer et al., 2019; Soligo et al., 2019). The flexibility and degree of detail of such high-fidelity (HF) calculations pro-

\* Corresponding author at: Department of Fluid Mechanics, Technical University of Catalonia – BarcelonaTech, Barcelona 08019, Spain.  
E-mail address: [lluis.jofre@upc.edu](mailto:lluis.jofre@upc.edu) (L. Jofre).

vides insightful information for the characterization of the underlying flow physics. In addition, the results obtained can be used as reference data for the development of coarse-grained models useful in the design and optimization of engineering systems. However, the computational cost of these fine-grained simulations are extraordinarily high, typically requiring large allocations in powerful computing facilities. In particular, the necessity of high-performance computing (HPC) resources arises from the stringent spatio-temporal resolutions required to capture for sufficient long periods of time, e.g., large-eddy turnover time in turbulence-dominated flows, the wide range of turbulent length and time scales (Moin and Mahesh, 1998; Tryggvason et al., 2013) and the temporal evolution of interfaces (Jofre et al., 2010; 2014; 2015; Valle et al., 2020) as they change topology and break-up/coalesce.

The computational cost of studying turbulence can be significantly reduced by means of large-eddy simulation (LES) approaches (Rogallo and Moin, 1984; Lesieur and Metais, 1996; Meneveau and Katz, 2000), in which the small-scale motions in the bulk of the flow are modeled (Jofre et al., 2018; 2019) instead of resolved. Although much less explored than in single-phase turbulence, the extension of LES strategies to multiphase flow problems started two decades ago marked by the gradual migration from Reynolds-Averaged Navier-Stokes (RANS) modeling to scale-resolving turbulence simulation including LES and its multiphase flow sub-variants (Lakehal, 2018): (i) dispersed-flow LES [referred to as large-eddy and structure simulation (LESS)], (ii) and interfacial-flow LES [referred to as large-eddy and interface simulation (LEIS)]. This transition was mainly driven by the limited predictive performance of statistical turbulence modeling in multiphase flows. The derivation of the LESS equations is detailed in the work by Lakehal et al. Lakehal et al. (2002), and the resulting formulation has been applied, based on two-fluid approaches (Crowe et al., 1996), to study bubbly flow (Deen et al., 2001), sprays (Sirignano, 2002), particle-laden flow (Capecehatro and Desjardins, 2013), and buoyant plumes (Yang et al., 2016). While the LESS variant is best suited for a range of problems in which one of the phases is dispersed in the other, LEIS (Lakehal, 2010) provides superior accuracy at expenses of higher computational costs by directly resolving the interface dynamics and turbulent motions down to the grid resolution. This work focuses on the study of two-phase flows in which the carrier and dispersed phases are separated by an interface and interact with each other. Consequently, the LEIS strategy is selected to develop the near-interface modeling approach due to its higher accuracy. Over the past years, different mathematical frameworks have been proposed within the LEIS formalism based on directly filtering the flow (Labourasse et al., 2007; Klein et al., 2019) and interfacial (Toutant et al., 2009; Herrmann, 2013) regions, and proposing appropriate subfilter scale (SFS) models (Klein et al., 2020; Saeedipour et al., 2019; Hasslberger et al., 2020) to represent the interface dynamics and stresses (Aniszewski et al., 2012; Saeedipour and Schneiderbauer, 2019). LEIS has been applied, for example, to calculate turbulent gas-liquid flows involving large-scale sheared interfaces (Lakehal and Liovic, 2011), clustering of bubbles in wall-bounded flows (Lakehal, 2017), and primary breakup in atomization processes (Kaario et al., 2013).

Away from solid walls, LES has proven to be a computationally tractable approach to simulate single-phase, unsteady turbulent flows (Masquelet et al., 2017; Domino et al., 2019) over the past decades. However, as analyzed in a recent DNS study of isotropic turbulence laden with finite-size droplets by Dodd and Jofre (2019), the smallest hydrodynamic scales in turbulent two-phase flows are located at the interfacial regions, presenting characteristic sizes that are 2–3 times smaller than that of the dissipative Kolmogorov scales in the surrounding bulk flow. In particular, the flow topologies in these regions resemble those found in wall-

bounded flows. Therefore, to bypass the near-interface stringent resolution requirements and make LES approaches cost-efficient for the study of turbulent two-phase flows, this work focuses on the derivation of the theoretical framework and *a priori* analyses of interfacial layer flow models based on ideas inspired from wall-modeled LES approaches (Piomelli and Balaras, 2002; Kawai and Larsson, 2012). To that end, this paper is organized as follows. First, in Section 2, important dimensionless numbers and characteristic scales in two-phase turbulence are introduced. A description of the LES (filtered Navier–Stokes) equations is given in Section 3. In Section 4, the derivation of the near-interface flow modeling approach is presented. Next, in Section 5, performance tests and experiments are discussed. Finally, in Section 6, the work is concluded and future directions are proposed.

## 2. Dimensionless numbers and characteristic scales

The dynamics of multiphase flows is characterized by a variety of nondimensional numbers (Tryggvason et al., 2011; Jofre et al., 2020). Their importance depends on the physical mechanisms driving the flow. In turbulent flows, the ratio between inertial and viscous forces is characterized by the Reynolds number defined as

$$Re = \frac{\rho LU}{\mu} = \frac{LU}{\nu}, \quad (1)$$

where  $L$  and  $U$  are characteristic length and velocity scales, and  $\rho$ ,  $\mu$  and  $\nu = \mu/\rho$  are the density and dynamic and kinematic viscosities, respectively, of one of the phases. For inertia-dominated two-phase flows, pressure differences scale proportionally to  $\rho U^2$ , and as a result the normal stress condition at interfaces introduces the dimensionless Weber number expressing the ratio of inertia to surface tension forces given by

$$We = \frac{\rho LU^2}{\sigma}, \quad (2)$$

with  $\sigma$  the surface tension coefficient. Eliminating the velocity  $U$  between the Reynolds and Weber numbers results in the Ohnesorge number  $Oh = \mu/\sqrt{\rho\sigma L}$ , which compares viscous and capillary forces.

The Reynolds and Weber numbers define a two-dimensional (2-D) space where different turbulent two-phase regimes can be distinguished. Associated to the different regimes are a set of characteristic scales related to the energy cascade and break-up processes. As presented in the paragraphs below, the flow mechanisms describing their behavior are described by the turbulent eddy sizes and bubble/droplet length scales.

As conceptualized by Richardson's (statistically steady-state) view of the energy cascade for single-phase flows (Richardson, 1922), turbulence can be considered to be composed of eddies of different sizes  $\ell$ . The eddies in the largest-size range are characterized by the length scale  $\ell_0$ , which is comparable to the integral flow scale  $\mathcal{L} \approx 6\ell_0$ . These turbulent motions are relatively slow, but very energetic, dominated by inertial effects, and unstable. As a result, they break up, transferring their energy to somewhat smaller eddies. These smaller eddies undergo a similar break-up process, and transfer their energy to yet smaller eddies. This energy cascade continues down to the Kolmogorov scale  $\eta$  (Kolmogorov, 1941), where molecular diffusion is effective in dissipating the kinetic energy and stabilizing the flow motions. As illustrated in Fig. 1, the energy cascade can be separated in three distinct parts: (i) the energy-containing range where energy is introduced (production rate  $\mathcal{P}$ ), (ii) the inertial subrange in which energy is transferred to smaller eddies [transfer  $\mathcal{T}(\ell)$ ], and (iii) the dissipation range where viscous effects become dominant (dissipation rate  $\varepsilon$ ). The inertial subrange is delimited by the length scales  $\ell_{EI} \approx 1/6\ell_0$  and  $\ell_{DI} \approx 60\eta$ . The eddy size  $\ell_{EI}$

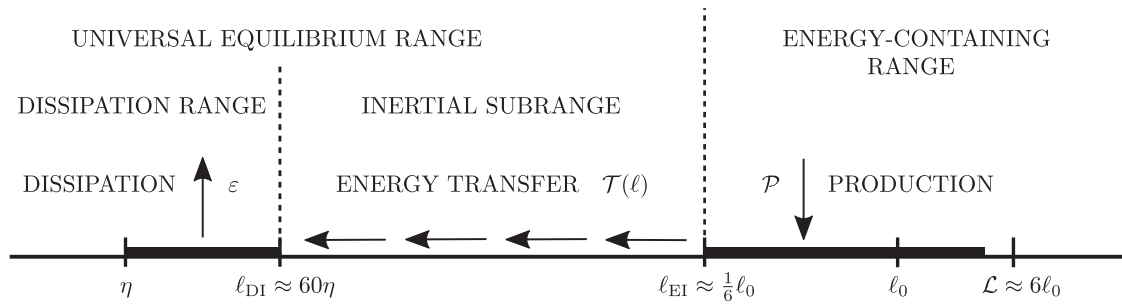


Fig. 1. Diagram of the energy cascade in terms of eddy sizes  $\ell$  (logarithmic scale) at very high Reynolds number showing the main turbulent scales and ranges. Illustration adapted from Pope (2000).

	Initial drop topology	Break-up morphology	Secondary droplets		Initial drop topology	Break-up morphology	Secondary droplets
No breakup $0 < We < 3$				Multimode $20 < We < 100$			
Vibrational $3 < We < 5$				Sheet stripping $100 < We < 350$			
Bag breakup $5 < We < 20$				Catastrophic $We > 350$			

Fig. 2. Classification of break-up morphologies and secondary droplet formation as function of the Weber number for gas-liquid systems ( $Oh < 0.1$ ). Graphics based on Pilch and Erdmann (1987).

demarcates the separation between the anisotropic large eddies ( $\ell > \ell_{EI}$ ) and the isotropic small eddies ( $\ell < \ell_{EI}$ ), whereas  $\ell_{DI}$  splits the universal equilibrium range between the inertial subrange ( $\ell_{EI} > \ell > \ell_{DI}$ ) and the dissipation range ( $\ell < \ell_{DI}$ ). In connection to LES approaches, in which the filter and grid sizes  $\Delta$  are expected to be sufficiently fine to resolve (approximately) 80% of the kinetic energy in the bulk of the phases (Pope, 2000), the length scale  $\ell_{EI}$  provides the theoretical maximum LES resolution by satisfying  $\Delta < \ell_{EI}$ .

In the case of multiphase flows with small Ohnesorge numbers ( $Oh < 0.1$ ), such as gas-liquid systems, the importance of viscous forces is relatively small and the Weber number becomes the principal parameter describing break-up behavior. For initially spherical drops, various break-up morphologies have been observed as a function of  $We = \rho_c U^2 D / \sigma$ , including vibrational, bag, bag-and-stamen, multimode, sheet-thinning and catastrophic modes, where  $\rho_c$  is the density of the carrier phase,  $D$  is the diameter of the dispersed phase, and  $U$  is the relative velocity between phases. Following the work by Pilch and Erdmann (1987), the break-up morphology classification of drops based on  $We$ , or liquid columns viewed from the top, and secondary droplet formation is depicted in Fig. 2. The no break-up condition is defined by cases where the drop stays intact, while the drop breaks into few large droplets in vibrational mode. Bag break-up is generally characterized by the occurrence of a single bag-like shape. If more than one bag is formed, the morphology is considered multimode. Finally, sheet stripping and catastrophic break-up occur when the edges of the drop are accelerated and separated from the main body faster than the volumetric core. As shown in the figure, the break-up morphology determines the distribution of the secondary droplets generated from vortical and straining fragmentation mechanisms. The droplet size at which the break-up process ends, due to the balance between fragmentation and surface tension forces, corresponds to

the Hinze scale Kolmogorov (1949); Hinze (1955) defined as

$$R_H \sim \left( \frac{\sigma}{\rho_c} \right)^{3/5} \varepsilon^{-2/5}. \quad (3)$$

The set of dimensionless numbers  $Re$ ,  $We$  and characteristic scales  $\ell_{EI}$ ,  $\eta$ ,  $R_H$  are utilized to construct the regime diagram presented in Fig. 3 for turbulent flows laden with a finite-size dispersed phase. The strategy chosen in this work to perform simulations of two-phase turbulence is based on the LEIS approach. The particular methodology developed captures interfaces (topology deformations and break-up processes) on the computational mesh by selecting the grid resolution to be in the order of the Hinze scale, while filters the small-scale turbulent fluctuations in the bulk of the phases. In addition, as described in Section 4 and assessed in Section 5, viscous near-interface flow motions are modeled instead of resolved to maintain the cost-efficiency of the LEIS approach. In contrast to LES strategies in which the flow and interfaces are filtered (Labourasse et al., 2007; Toutant et al., 2009; Herrmann, 2013), resulting in (potentially) large computational savings at expenses of significantly complex mathematical formulations and closure models, the approach presented in this work, although (presumably) more expensive by construction, is designed to be efficient in a large portion of the  $Re - We$  diagram (yellow/green color region) by balancing computational cost, modeling complexity and accuracy.

For illustration purposes<sup>1</sup>, Fig. 3 is constructed by considering homogeneous isotropic turbulence (HIT) laden with finite-size

<sup>1</sup> The Taylor microscale is mathematically defined between the Kolmogorov and integral length scales, and has been consequently selected as a representative example within the range of applicability envisioned for the modeling approach. Other length scales in the inertial subrange could be considered for generating the regime diagram, resulting only in small variations of the location of the separation lines.

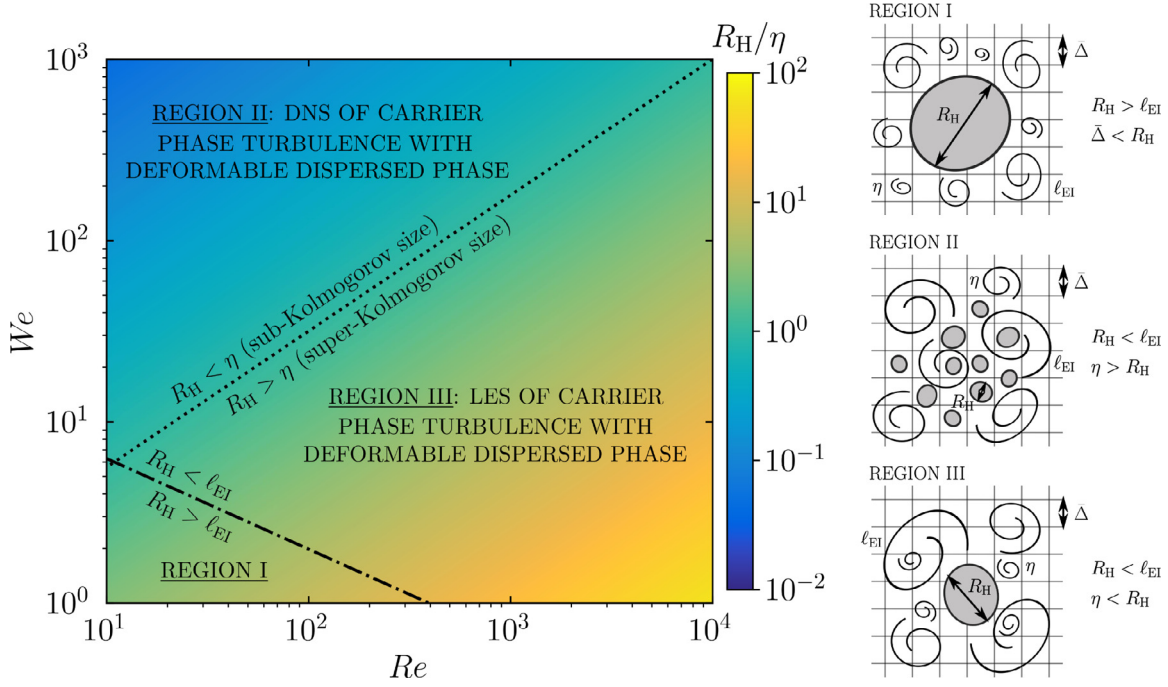


**Fig. 3.**  $Re - We$  DNS/LES regime diagram of carrier phase turbulence for HIT laden with finite-size droplets/bubbles. Size of dispersed phase is assumed to be in the order of the Taylor microscale for illustration purposes. The schematics (right column) represent the comparison of hydrodynamic, dispersed and computational scales for the three different regions identified.

droplets/bubbles with characteristic diameters in the order of the Taylor microscale  $\lambda$ , and with relative velocities determined by the root-mean-square (rms) turbulent fluctuations  $U_{rms}$ . Under such assumptions, and knowing that for HIT the ratio between Kolmogorov and largest-size scales is  $\eta/\ell_0 \sim Re^{-3/4}$  and the dissipation rate is given by  $\varepsilon = 15\nu U_{rms}^2/\lambda^2$  (Pope, 2000), the following relations between dimensionless numbers and characteristic scales are obtained

$$R_H/\eta \sim Re^{9/20}We^{-3/5} \quad \text{and} \quad R_H/\ell_{EI} \sim Re^{-3/10}We^{-3/5}. \quad (4)$$

These expressions are utilized to demarcate three different regions in the  $Re - We$  diagram. The first region (I) is named “LES of Carrier Phase Turbulence with Quasi-Non-Deformable Dispersed Phase” and corresponds to  $R_H > \ell_{EI}$ , where  $We$  is small and the resulting interfacial structures could be captured with relatively coarse grids. However, the condition  $\bar{\Delta} < \ell_{EI}$  imposes finer resolutions. This is a region where immersed boundary methods (IBM) are typically used for DNS studies (Mittal and Iaccarino, 2005; Lucci et al., 2010). In the second region (II), termed “DNS of Carrier Phase Turbulence with Deformable Dispersed Phase” and given by  $R_H < \ell_{EI}$  &  $R_H < \eta$ ,  $We$  is considerably larger than  $Re$ , and as a result the dynamics of the dispersed phase is dominated by break-up processes. Consequently, interface-resolving simulations are exceedingly expensive, and instead methodologies based on sub-filter and/or sub-Hinze-scale modeling should be considered. Finally, the third region (III) is defined by  $\eta < R_H < \ell_{EI}$  and referred to as “LES of Carrier Phase Turbulence with Deformable Dispersed Phase”. This portion of the diagram is where our present strategy is envisioned to be efficient since the mesh required to capture interfaces (down to the Hinze scale) corresponds to a LES resolution in the bulk of the phases, i.e.,  $\bar{\Delta} \sim R_H$ . Therefore, the combination of a coarser grid resolution and the modeling of the viscous near-interface flow motions could result in significant computational savings within the LEIS approach.

### 3. Large-eddy simulation equations

At isothermal conditions without phase change, the nondimensional equations of fluid motion describing immiscible two-phase incompressible flow are the continuity and Navier–Stokes equations given as Tryggvason et al. (2011)

$$\nabla \cdot \mathbf{u} = 0, \quad (5)$$

$$\frac{\partial \mathbf{u}}{\partial t} + \nabla \cdot (\mathbf{u}\mathbf{u}) = \frac{1}{\rho} \left[ -\nabla p + \frac{1}{Re} \nabla \cdot (2\mu\mathbf{S}) + \frac{1}{We} \mathbf{f}_\sigma \right], \quad (6)$$

where  $\mathbf{u}$  and  $p$  are the velocity and pressure of the flow,  $\rho$  and  $\mu$  are the piecewise step functions of density and viscosity for the one-fluid system,  $\mathbf{S} = [\nabla\mathbf{u} + (\nabla\mathbf{u})^T]/2$  is the strain-rate tensor, and  $\mathbf{f}_\sigma = \kappa\mathbf{n}_\Sigma\delta(\mathbf{x} - \mathbf{x}_\Sigma)$  is the force per unit volume due to surface tension with  $\kappa = -\nabla \cdot \mathbf{n}_\Sigma$  and  $\mathbf{n}_\Sigma$  the interface curvature and normal vector, respectively, and  $\delta(\mathbf{x} - \mathbf{x}_\Sigma)$  the Dirac delta function concentrated at the interface location  $\mathbf{x}_\Sigma$ , which evolves according to the velocity field as

$$\frac{d\mathbf{x}_\Sigma}{dt} = \mathbf{u}(\mathbf{x}_\Sigma, t). \quad (7)$$

The derivation of this set of one-fluid conservation equations assumes that the interface is sharp with respect to the hydrodynamic flow scales, and consequently the following nondimensional interfacial jump conditions are satisfied implicitly

$$[\rho]_\Sigma = \rho_2 - \rho_1 \quad \text{and} \quad [\mu]_\Sigma = \mu_2 - \mu_1, \quad (8)$$

$$[\mathbf{u}]_\Sigma = 0 \quad \text{and} \quad \left[ -p + \frac{1}{Re} \mathbf{n}_\Sigma \cdot 2\mu\mathbf{S} \cdot \mathbf{n}_\Sigma \right]_\Sigma = -\frac{1}{We} \kappa, \quad (9)$$

with subscripts 1, 2 and  $\Sigma$  denoting phase/fluid 1 and 2 and the interface between them, respectively.

The LES equations are derived by applying a low-pass filter  $G$  to the equations of fluid motion. The filter decomposes any flow

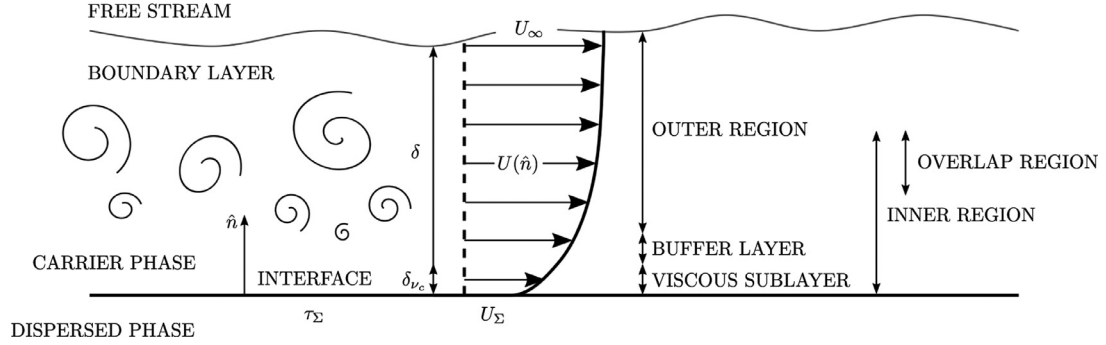


Fig. 4. Schematics and notation of a fully-developed interfacial boundary-layer.

variable  $\phi(\mathbf{x}, t)$  into large- $\bar{\phi}$  and small-scale  $\phi'$  contributions, i.e.,  $\phi = \bar{\phi} + \phi'$ . The filtered part is defined as

$$\bar{\phi}(\mathbf{x}, t) = \int_{\Omega} G(\mathbf{x}, \mathbf{x}', \Delta) \phi(\mathbf{x}', t) d\mathbf{x}', \quad (10)$$

with  $\mathbf{x}$  and  $\mathbf{x}'$  position vectors in the domain  $\Omega$ , and  $\Delta$  the characteristic width of the filter. However, as introduced in Section 2, the methodology chosen in this work to perform scale-resolving studies of two-phase turbulence is based on a particular version of the LEIS approach such that the small flow scales in the bulk of the phases are filtered, while interfaces are captured. Therefore, the approach proposed is envisioned to be efficient in Region III of Fig. 3, and with filter sizes between the Kolmogorov and Hinze scales. Under this assumption, the filtered interface evolution equation takes the form

$$\frac{d\mathbf{x}_{\Sigma}}{dt} = \bar{\mathbf{u}}(\mathbf{x}_{\Sigma}, t), \quad (11)$$

and, since the interface topology is captured and the right-hand sides involve no velocity terms, the filtered interfacial jump conditions become

$$[\bar{\rho}]_{\Sigma} = \rho_2 - \rho_1 \quad \text{and} \quad [\bar{\mu}]_{\Sigma} = \mu_2 - \mu_1, \quad (12)$$

$$[\bar{\mathbf{u}}]_{\Sigma} = 0 \quad \text{and} \quad \left[ -p + \frac{1}{Re} \mathbf{n}_{\Sigma} \cdot 2\mu \mathbf{S} \cdot \mathbf{n}_{\Sigma} \right]_{\Sigma} = -\frac{1}{We} \sigma \mathcal{K}. \quad (13)$$

Finally, assuming that differentiation and filtering commute (Vasilyev et al., 1998; Marsden et al., 2002), the filtered continuity and Navier–Stokes equations result in

$$\nabla \cdot \bar{\mathbf{u}} = 0, \quad (14)$$

$$\frac{\partial \bar{\mathbf{u}}}{\partial t} + \nabla \cdot (\bar{\mathbf{u}} \bar{\mathbf{u}}) = \frac{1}{\rho} \left[ -\nabla \bar{p} + \frac{1}{Re} \nabla \cdot (2\mu \bar{\mathbf{S}}) + \frac{1}{We} \mathbf{f}_{\sigma} \right] - \nabla \cdot \boldsymbol{\tau}, \quad (15)$$

where, following Leonard's decomposition (Leonard, 1974),  $\boldsymbol{\tau} = \bar{\mathbf{u}} \bar{\mathbf{u}} - \bar{\mathbf{u}} \bar{\mathbf{u}}$  is the SFS, or turbulent, stress tensor. The resolved scales of LES  $\bar{\phi}$  are characterized by the filter applied to the conservation equations. In a general context, the filtering and discretization operators are different (Lund, 2003). However, in most cases the spatial discretization is chosen to be specifically the low-pass filter (Rogallo and Moin, 1984), and therefore  $\boldsymbol{\tau}$  is habitually referred to as the subgrid-scale (SGS) tensor. Based on the particularization of the work by Sagaut and Germano (2005) to incompressible two-phase flows with no phase change,  $\boldsymbol{\tau}$  is not altered due to the interfacial discontinuity since  $[\mathbf{u}]_{\Sigma} = 0$ , only (potentially) by the modulation of turbulence resulting from the interaction between the dispersed and carrier phases as discussed in Sections 4 and 5.

#### 4. Near-interface flow modeling

The Kolmogorov scale, as described in Section 2, characterizes the smallest flow motions in single-phase unbounded turbulence. In the case of two-phase systems, however, the discrete phase introduces (potentially smaller) additional scales through two main mechanisms: (i) deformation and break-up processes, and (ii) velocity gradients and wakes in the vicinity of interfaces. For example, the formation of ligaments and films (Martínez-Bazán et al., 1999) with sizes determined by the Hinze scale, and boundary-layer-like flow structures (Dodd and Jofre, 2019) with thicknesses dependent on the material and flow properties of the different phases/fluids.

In this section, since the LEIS approach proposed is designed to capture the evolution of interfaces down to the Hinze scale, the near-interface flow modeling is focused on the coarse-grained representation of the small-scale, sheared flow motions generated at the interfacial regions to largely improve the cost-effectiveness of the calculations. In particular, the recent work by Dodd and Jofre (2019) quantified that the DNS of HIT laden with finite-size droplets requires an order of magnitude larger number of grid points than its single-phase counterpart. Therefore, similar to LES of wall-bounded flows in which models (or special boundary conditions) are required to reduce the stringent resolution requirements in the viscous near-wall region, the paragraphs below will explore the extension of wall modeling approaches (Piomelli and Balaras, 2002; Kawai and Larsson, 2012) to two-phase turbulent flows.

The first step is to connect boundary-layer theory (Schlichting and Gersten, 2016) with the flow structure near interfaces. Following Csanady's slip wall approach (Csanady, 1997), let us consider the mean velocity distribution in the vicinity of an approximately flat interface<sup>2</sup> assuming fully-developed steady-state conditions, in the absence of inertial fluctuations, and with uniform shear stress in the interface-normal direction. As sketched in Fig. 4, let the interfacial boundary layer be conceptually divided into an inner and outer region such that:

1. In the inner region, the mean velocity profile  $U(\hat{n})$  and turbulence statistics are presumed to depend only on the distance from the interface  $\hat{n}$ , the kinematic viscosity of the carrier phase  $\nu_c = \mu_c/\rho_c$ , and the interfacial shear stress

$$\tau_{\Sigma} = \sqrt{(\mathbf{t}_1 \cdot 2\mu \mathbf{S} \cdot \mathbf{n}_{\Sigma})^2 + (\mathbf{t}_2 \cdot 2\mu \mathbf{S} \cdot \mathbf{n}_{\Sigma})^2}, \quad (16)$$

where  $\mathbf{t}_1$  and  $\mathbf{t}_2$  are two orthogonal unit vectors that are tangent to the interface. Note that in the absence of surface tension gradients (no Marangoni stresses) the shear stress is continuous across

<sup>2</sup> In HIT laden with finite-size droplets, based on DNS studies by Dodd and Jofre (2019), the ratio between cross-sectional perimeter and mean boundary-layer thickness is  $\pi D_0/\delta \sim 20$ .

the interface, i.e.,  $\tau_\Sigma = \tau_{\Sigma c} = \tau_{\Sigma d}$ . In addition,  $\tau_\Sigma$  is utilized to characterize the friction velocity  $u_{\tau_\Sigma} \equiv \sqrt{\tau_\Sigma/\rho_c}$  and viscous length scale  $\delta_{\nu c_\Sigma} \equiv \nu_c \sqrt{\rho_c/\tau_\Sigma} = \nu_c/u_{\tau_\Sigma}$ , and nondimensionalize the variables  $U^+ \equiv U/u_{\tau_\Sigma}$  and  $\hat{n}^+ \equiv \hat{n}u_{\tau_\Sigma}/\nu_c$  on the carrier-phase side of the interface. Upon dimensional analysis it can be shown that the relative velocity  $U_r^+ \equiv U^+ - U_\Sigma^+$ , with  $U_\Sigma^+ \equiv U_\Sigma/u_{\tau_\Sigma}$  the interface velocity in viscous units, is of the form

$$U_r^+ \equiv U^+ - U_\Sigma^+ = f(\hat{n}^+). \quad (17)$$

This inner region is composed of: (i) the viscous sublayer ( $0 < \hat{n}^+ < 5$ ) where turbulent fluctuations are suppressed, molecular viscosity dominates momentum transport, and the relative velocity increases linearly with distance from the interface, i.e.,  $U_r^+ \equiv U^+ - U_\Sigma^+ = \hat{n}^+$ ; (ii) the log-law region ( $\hat{n}^+ > 30$ ), which overlaps with the outer region and where momentum transport is dominated by turbulent fluctuations (Reynolds stresses); and (iii) a buffer layer ( $5 < \hat{n}^+ < 30$ ) transitional between (i) and (ii). The inner region extends from the interface to an approximate distance of  $\hat{n} \approx 0.15\delta$ , where  $\delta$  is the thickness of the boundary layer defined by the location in which the flow velocity is 99% of the free stream velocity  $U_\infty$ , i.e.,  $U(\delta) = 0.99U_\infty$ .

2. In the outer region, the mean velocity profile and turbulence statistics depend on the friction velocity  $u_{\tau_\Sigma}$  and the boundary layer thickness  $\delta$ , but not on the kinematic viscosity  $\nu_c$  (momentum transport is entirely dominated by Reynolds stresses), and therefore is function of

$$U_\infty^+ - U^+ = g\left(\frac{\hat{n}}{\delta}\right). \quad (18)$$

The outer region extends the region  $30/Re_{\tau_\Sigma} < \hat{n}/\delta < 1$ , with the friction Reynolds number  $Re_{\tau_\Sigma} \equiv u_{\tau_\Sigma}\delta/\nu_c$  characterizing the ratio between the outer  $\delta$  and inner  $\delta_{\nu c_\Sigma}$  region length scales.

3. In the overlap region, where the inner and outer regions meet, an asymptotic matching argument based on Eqs. (17) and (18) (similar to Millikan's analysis (Millikan, 1939)) implies the existence of a logarithmic relationship between the mean velocity and distance from the interface expressed as

$$U^+ - U_\Sigma^+ = \frac{1}{\kappa} \ln \hat{n}^+ + A^+ \quad \text{for } \hat{n}/\delta_{\nu c_\Sigma} \rightarrow \infty \quad (\text{inner region}), \quad (19)$$

$$U_\infty^+ - U^+ = -\frac{1}{\kappa} \ln \frac{\hat{n}}{\delta} + B^+ \quad \text{for } \hat{n}/\delta \rightarrow 0 \quad (\text{outer region}), \quad (20)$$

where  $\kappa \approx 0.41$  is the von Kármán constant, and  $A^+$  and  $B^+$  are parameters that depend on the details of the interface and the flow field, respectively. For example, in the case of solid boundaries,  $A^+ \approx 5$  for smooth surfaces and  $B^+ \approx 2.3$  for zero-pressure-gradient flows. Adding these two equations yields the slip law

$$U_\infty^+ - U_\Sigma^+ = \frac{1}{\kappa} \ln Re_{\tau_\Sigma} + A^+ + B^+. \quad (21)$$

Once the classical boundary-layer theory has been adapted to interfacial flows, the final step is to propose a modeling strategy for the near-interface region. As introduced in the sections above, in this work we explore the utilization/extension of approaches developed for wall-stress modeling. Many different methodologies have been proposed in the past decades with the aim of representing various boundary-layer phenomena and with different balances between accuracy and computational cost; see, for example, the recent review by Bose and Park (2018) for a detailed exposition. However, as a first analysis of this problem, we focus on a simple model in which the interfacial shear stress is algebraically related to the velocity at some distance  $\hat{n}^*$  from the interface; in algebraic closures, it is typically assumed that the law of the wall is valid locally and instantaneously, and a no-penetration condition is enforced for the wall-normal velocity. In the absence of pressure-gradient effects on the boundary layer, the LES velocity profile can

be assumed to satisfy a logarithmic law (Deardoff, 1970) in the form

$$\bar{u}(\hat{n}^*) - u_\Sigma = u_{\tau_\Sigma}^{\text{IM}} \left[ \frac{1}{\kappa} \ln \left( \frac{\hat{n}^* u_{\tau_\Sigma}^{\text{IM}}}{\nu_c} \right) + C^+ \right], \quad (22)$$

where  $u_\Sigma$  and  $u_{\tau_\Sigma}^{\text{IM}}$  are the unknown interface and interface-modeled (denoted by superscript IM) friction velocities, respectively, and  $C^+$  is a normalized intercept coefficient particular to the problem. The modeling strategy therefore is to utilize the equation above to prescribe the velocity profile near the interface. The problem, however, is that there is one equation (Eq. (22)) and two unknowns ( $u_\Sigma$  and  $u_{\tau_\Sigma}^{\text{IM}}$ ) rendering the system undetermined. To remediate this problem, it is assumed that  $u_\Sigma$  is dominated by the resolved (large) scales, and consequently it can be approximated from the LES velocity at the grid point capturing the interface, i.e.,  $u_\Sigma \approx \bar{u}_{\hat{n}=0}$ ; the implicit assumption is that the kinetic energy of the inner region is much smaller than that of the outer region. Once  $u_\Sigma$  is obtained, the system is determined and the LES velocity at a matching location  $\hat{n}^*$  in the range  $30 < \hat{n}^+ < 0.15Re_{\tau_\Sigma}$  is utilized to iteratively approximate  $u_{\tau_\Sigma}^{\text{IM}}$  from Eq. (22).

## 5. Numerical experiments

This study uses results from DNS of droplet-laden decaying HIT (Dodd and Ferrante, 2016). These simulations used the volume-of-fluid (VoF) method to resolve the flow inside and outside the droplets and modeled the surface tension effects. A full description of the numerical methods that were used to simulate the turbulent two-phase flow is provided in references (Baraldi et al., 2014; Dodd and Ferrante, 2014).

### 5.1. Initial conditions and droplet properties

As detailed in Dodd and Ferrante (2016), the system is initialized at  $t = 0$  with a velocity field generated by prescribing the turbulent kinetic energy (TKE) spectrum, ensuring that the initial random velocity field is isotropic and divergence-free, and that the velocity cross-correlation spectra satisfy the realizability conditions (Schumann, 1977). The Reynolds number  $Re_{\text{ref}} = \rho_{\text{ref}} U_{\text{ref}} L_{\text{ref}} / \mu_{\text{ref}} = 6.42 \times 10^4$  based on the density  $\rho_{\text{ref}} = \rho_c = 1 \text{ kg/m}^3$  and viscosity  $\mu_{\text{ref}} = \mu_c = 1.33 \times 10^{-5} \text{ m}^2/\text{s}$  of the carrier phase, the reference velocity  $U_{\text{ref}} = 26.7 \text{ m/s}$ , and the HIT domain size  $L_{\text{ref}} = 3.2 \times 10^{-2} \text{ m}$ , is utilized to nondimensionalize the problem. After one dimensionless time unit, defined as  $t \equiv L_{\text{ref}}/U_{\text{ref}}$ , the droplets are introduced into the system with zero velocity and set free to interact with the turbulent flow field.

Table 1 shows the dimensionless flow parameters at different times  $t$  for the droplet-free flow (case A), where  $U_{\text{rms}}$  is the root-mean-square (rms) turbulent fluctuations,  $\varepsilon$  is the dissipation rate,  $\ell_0 \approx \mathcal{L}/6$  and  $\tau_{\ell_0}$  are comparable to the integral length and time scales,  $\lambda$  is the Taylor length scale,  $Re_\lambda = U_{\text{rms}}\lambda/\nu_c$  and  $Re = (3/20)Re_\lambda^2$  are the Reynolds number based on the Taylor and integral scales, respectively, and  $\eta$  and  $\tau_\eta$  are the Kolmogorov length and time scales. The initial turbulent flow field is well resolved, as indicated by  $\kappa_{\text{max}}\eta = 4.3$  at  $t = 0$ , where  $\kappa_{\text{max}} = \pi N$  is the maximum resolved wavenumber and  $N = 1024$  is the number of grid points in each direction of the computational grid.

The dataset contains one simulation (case A) of droplet-free flow and eight simulations (A\*–H) of droplet-laden isotropic turbulence corresponding to the cases listed in Table 2. Case A\* is a limiting case in which the viscosity and density ratios are unity and the Weber number of the droplets is infinity. We analyze the effects of varying the initial droplet Weber number ( $We = \rho_c D_0 U_{\text{rms}}^2 / \sigma$ ), droplet- to carrier-fluid density ratio ( $\varphi = \rho_d / \rho_c$ ),

**Table 1**

Flow parameters (dimensionless) at initial time ( $t = 0$ ), droplet release time ( $t = 1$ ), time at which the solution is independent of the initial conditions ( $t = 2.5$ ), and final time ( $t = 6$ ) in case A.

$t$	$U_{rms}$	$\varepsilon$	$\ell_0$	$\lambda$	$\eta$	$Re$	$Re_\lambda$	$\ell_0/\eta$	$\tau_{\ell_0}$	$\tau_\lambda$	$\tau_\eta$
0.0	0.0509	$1.15 \times 10^{-3}$	0.0965	0.0229	$1.35 \times 10^{-3}$	844	75	71.7	1.89	0.45	0.116
1.0	0.0457	$6.10 \times 10^{-4}$	0.1038	0.0283	$1.58 \times 10^{-3}$	1036	83	65.8	2.27	0.62	0.160
2.5	0.0397	$4.49 \times 10^{-4}$	0.1030	0.0286	$1.70 \times 10^{-3}$	784	72	60.5	2.60	0.72	0.186
6.0	0.0285	$2.18 \times 10^{-4}$	0.1082	0.0295	$2.04 \times 10^{-3}$	437	54	53.0	3.80	1.04	0.268

**Table 2**

Droplet properties (dimensionless) at release time  $t = 1.0$ .

Case	$We$	$\varphi \equiv \rho_d/\rho_c$	$\gamma \equiv \mu_d/\mu_c$	$\tau_d$	$\tau_d/\tau_{\ell_0}$	$\tau_d/\tau_\eta$
A	-	-	-	-	-	-
A*	$\infty$	1	1	-	-	-
B	0.1	10	10	35.9	15.8	225
C	1.0	10	10	35.9	15.8	225
D	5.0	10	10	35.9	15.8	225
E	1.0	1	10	3.6	1.6	23
F	1.0	100	10	359.0	158.0	2250
G	1.0	10	1	41.8	18.4	261
H	1.0	10	100	34.9	15.4	219

**Table 3**

Viscous scaling parameters (dimensionless) at  $t = 2.5$ :  $\tau_\Sigma$  is the shear stress at the interface,  $u_{\tau_\Sigma}$  is the interfacial friction velocity in the carrier phase,  $\delta_{v_{c\Sigma}}$  is the interfacial viscous length scale in the carrier phase, and  $\delta_{v_{c\Sigma}}/\delta_{v_c}$  is the interfacial viscous length scale in the carrier phase normalized by the mean viscous length scale of the carrier phase.

Case	$\tau_\Sigma$	$u_{\tau_\Sigma}$	$\delta_{v_{c\Sigma}}$	$\delta_{v_{c\Sigma}}/\delta_{v_c}$
A*	$4.85 \times 10^{-5}$	$6.96 \times 10^{-3}$	$2.24 \times 10^{-3}$	1.020
B	$2.45 \times 10^{-4}$	$1.57 \times 10^{-2}$	$9.94 \times 10^{-4}$	0.453
C	$2.41 \times 10^{-4}$	$1.55 \times 10^{-2}$	$1.00 \times 10^{-3}$	0.458
D	$2.33 \times 10^{-4}$	$1.53 \times 10^{-2}$	$1.02 \times 10^{-3}$	0.465
E	$1.77 \times 10^{-4}$	$1.33 \times 10^{-2}$	$1.17 \times 10^{-3}$	0.533
F	$3.40 \times 10^{-4}$	$1.84 \times 10^{-2}$	$8.45 \times 10^{-4}$	0.385
G	$1.40 \times 10^{-4}$	$1.18 \times 10^{-2}$	$1.31 \times 10^{-3}$	0.599
H	$3.40 \times 10^{-4}$	$1.84 \times 10^{-2}$	$8.45 \times 10^{-4}$	0.386

and droplet- to carrier-fluid viscosity ratio ( $\gamma = \mu_d/\mu_c$ ) in the three sets BCD, CEF, and CGH, respectively, while keeping the other two parameters constant. In cases B, C, and D,  $We$  increases from 0.1 to 5.0 by decreasing the surface tension coefficient. In cases C, E, and F,  $\varphi$  increases from 1 to 100 by increasing  $\rho_d$ . In cases C, G, and H,  $\gamma$  increases from 1 to 100 by increasing  $\mu_d$ . For all cases, the droplet volume fraction is  $\alpha_v = 0.05$ , the initial number of droplets is  $N_d = 3130$ , and the initial nondimensional droplet diameter is  $D_0 = 0.03125$ , which is equal to  $20\eta_{t=1}$  (or equivalently  $1.1\lambda_{t=1}$ ), where  $\eta_{t=1}$  and  $\lambda_{t=1}$  are the Kolmogorov and Taylor length scales at the time the droplets are released in the flow ( $t = 1$ ). This yields a droplet resolution of 32 grid points per diameter.

## 5.2. Conditional averaging methodology

Motivated by studying the flow structure near the droplet surface, we introduce a conditional averaging procedure to compute statistical quantities conditioned on distance from the interface. Starting with the VoF field, we use the marching cubes algorithm (Lewiner et al., 2003) to compute a level set (LS), or signed distance function, representing the shortest distance to the interface, which has the property  $\phi = 0$  at the interface,  $\phi < 0$  in the droplet fluid, and  $\phi > 0$  in the carrier fluid. Fig. 6 shows the VoF and LS fields in an  $x$ - $y$  plane at  $t = 2.5$ . Note that the computational cost of the algorithm to compute  $\phi$  scales as  $(|\phi|_{\max}N)^3$ , where  $|\phi|_{\max}$  is the maximum search distance for computing  $\phi$  and  $N$  is the number of grid points in each spatial direction. There-

fore, to limit the computational cost, while still capturing most of the inner region of the interfacial boundary layers, we set  $|\phi|_{\max}$  to approximately two to three droplet diameters depending on the relative position of the neighboring droplets. This limitation explains the white regions in Fig. 6(b).

## 5.3. Viscous scales

We have defined in Section 4 the viscous scales that characterize the magnitude of the velocities and length sizes near the droplet surface. These scales serve as (i) a measure of the smallest hydrodynamic scales at the droplet surface, and (ii) a reference value for expressing the quantities in viscous units. A fundamental question we aim to address is how does  $\delta_{v_{c\Sigma}}$  compare to the smallest length scale of the surrounding turbulent flow, i.e., the Kolmogorov scale of the carrier phase  $\eta_c$ . To make the comparison direct, we compute the viscous length scale of the carrier phase  $\delta_{v_c} = \nu_c \sqrt{\rho_c/\tau_c}$ , where the mean shear stress for canonical decaying isotropic turbulence is  $\tau_c = \mu_c \sqrt{(4\varepsilon_c)/(15\nu_c)}$  (Pope, 2000). Note that, in this context,  $\delta_{v_c}$  is simply an alternative definition of the Kolmogorov scale. The relationship between  $\delta_v$  and  $\eta$  is  $\delta_v = (15/4)^{1/4}\eta \approx 1.39\eta$ .

Table 3 shows that  $\delta_{v_{c\Sigma}}/\delta_{v_c}$  in case A\* is close to unity as would be expected for canonical decaying HIT, which indicates that the effect of initial conditions is undetectable at  $t = 2.5$ . If we compare  $\delta_{v_{c\Sigma}}/\delta_{v_c}$  for case A\* to the droplet-laden cases B–H,  $\delta_{v_{c\Sigma}}/\delta_{v_c}$  for the droplet-laden cases is consistently one-third to one-half as large. Fig. 7 shows the time evolution of  $\delta_{v_{c\Sigma}}$  normalized by  $\delta_{v_c}$ . For all cases and all times,  $\delta_{v_{c\Sigma}}/\delta_{v_c}$  is less than unity, therefore the smallest length scale is always located at the droplet surface due to the induced velocity gradient. Looking at the time evolution of  $\delta_{v_{c\Sigma}}/\delta_{v_c}$ , we recall that the droplets are released from rest at  $t = 1$ , leading to an instantaneous increase in  $\tau_\Sigma$  which explains the minimum in  $\delta_{v_{c\Sigma}}/\delta_{v_c}$ . However, after roughly one integral time scale ( $t \geq 1 + \tau_\ell \approx 2.8$ ),  $\delta_{v_{c\Sigma}}/\delta_{v_c}$  reaches a quasi-stationary value, suggesting that the effect of the initial conditions is forgotten.

The effects of varying  $We$ ,  $\varphi$ , and  $\gamma$  on  $\delta_{v_{c\Sigma}}$  are as follows. Fig. 7(a) shows that as  $We$  increases  $\delta_{v_{c\Sigma}}/\delta_{v_c}$  increases. The decrease in  $\delta_{v_{c\Sigma}}/\delta_{v_c}$  for case B at later times is explained by droplet coalescence. Droplet coalescence produces velocity fluctuations at the droplet scale through the power of the surface tension, and because the interfacial surface energy scales as  $We^{-1}$ , the effect is most pronounced for the lowest Weber number case B ( $We = 0.1$ ). As the density ratio increases, depicted in Fig. 7(b),  $\delta_{v_{c\Sigma}}/\delta_{v_c}$  decreases, showing that higher inertia droplets have larger velocity gradients and smaller length scales near their surfaces than lighter droplets. Fig. 7(c) shows that increasing the viscosity ratio  $\gamma$  leads to a decrease in  $\delta_{v_{c\Sigma}}/\delta_{v_c}$ . This suggests that in the solid particle limit ( $\gamma \rightarrow \infty$ ),  $\delta_{v_{c\Sigma}}/\delta_{v_c}$  would be minimum, implying that, from a computational perspective, solid particles are the most costly dispersed medium to simulate in terms of resolving the velocity gradient near the particle surface.

After one integral time scale,  $\delta_{v_{c\Sigma}}/\delta_{v_c}$  ranges between 0.35 and 0.5 depending on the case, indicating that  $\delta_{v_{c\Sigma}}$  is two to three times smaller than the smallest length scale in the surrounding turbulent flow. Consequently, to perform fully-resolved DNS of

**Table 4**

Hinze scale (dimensionless) and its ratio with the characteristic turbulent and LES length scales at  $t = 2.5$  with  $\rho_c = 1$  and  $\epsilon = 4.49 \times 10^{-4}$ .

Case	$R_H$	$R_H/\eta$	$R_H/\ell_{EI}$	$R_H/\ell_0$
A*	0	0	0	0
B	$2.26 \times 10^{-1}$	132.94	13.14	2.19
C	$5.68 \times 10^{-2}$	33.41	3.30	0.55
D	$2.16 \times 10^{-2}$	12.71	1.26	0.21
E	$5.68 \times 10^{-2}$	33.41	3.30	0.55
F	$5.68 \times 10^{-2}$	33.41	3.30	0.55
G	$5.68 \times 10^{-2}$	33.41	3.30	0.55
H	$5.68 \times 10^{-2}$	33.41	3.30	0.55

droplet-laden flows (ignoring breakup and coalescence for the time being), there is an additional microscale that must be resolved that is significantly smaller than the Kolmogorov scale. For the cases considered here, the number of grid points required on a fixed mesh is roughly ten to thirty ( $2^3$ – $3^3$ ) times larger than single-phase isotropic turbulence at the same Reynolds number. This fact, in part, explains why a numerical resolution of  $\kappa_{\max}\eta = 4.3$  was used to produce this DNS dataset.

#### 5.4. Hinze scales

The effect of the initial problem setup is forgotten at dimensionless time  $t \approx 2.5$ , as discussed in Section 5.3, when quasi-stationary conditions are achieved in terms of viscous scales. The analyses presented from this point forward, thus, will focus on the instantaneous dataset at  $t = 2.5$ .

The dataset considered in this work (cases B–H) is found in region III of the  $Re - We$  DNS/LES regime diagram introduced in Section 2 (at  $t = 2.5$ ,  $Re = 784$  and  $We$  ranges between 0.1 and 5), and is therefore suitable for exploring and assessing the performance of the near-interface flow modeling approach presented. The nondimensional value of the characteristic turbulent and LES length scales at  $t = 2.5$  for cases A\*–H correspond to  $\eta = 1.70 \times 10^{-3}$ ,  $\ell_{EI} = 1.72 \times 10^{-2}$ , and  $\ell_0 = 1.03 \times 10^{-1}$ , and the Hinze scale and associated ratios are listed in Table 4. The ratio between Hinze and anisotropic turbulent scales is  $R_H/\ell_{EI} \sim \mathcal{O}(1 - 10)$ , indicating that LES meshes with resolutions in the order of  $\ell_{EI}$  would be sufficient to capture the evolution of the interfaces down to the Hinze scale. In addition, from a spatial resolution perspective, the resulting LES mesh combined with the modeling of the small scales in the interfacial boundary-layer regions would potentially reduce the computational cost of studying two-phase turbulence phenomena by three orders of magnitude since the ratio between Kolmogorov and anisotropic turbulent scales is  $\ell_{EI}/\eta \sim \mathcal{O}(10)$ .

#### 5.5. Assessment of the interfacial boundary-layer flow structure

The first step toward validating an interfacial flow modeling approach for LES is to characterize the flow structure in the vicinity of interfaces. For this objective, the DNS dataset extracted from cases B–H at dimensionless time  $t = 2.5$  is analyzed by considering the spatially-averaged velocity field in the near-interface regions. The procedure to obtain spatially-averaged velocities is composed of three steps: (i) for each grid point, calculate the level-set distance with respect to the closest interface as depicted in Fig. 6(b), (ii) spatially average the velocity field conditioned on the distance to the interface, as illustrated in Fig. 5, by making use of the level-set distance previously computed, and (iii) decompose the resulting spatially-averaged velocity vectors into normal and tangential parts with respect to the interface to extract the tangential component  $U^+$ . In particular, focus is placed on the characteristics of the interfacial boundary layers generated by the interaction between

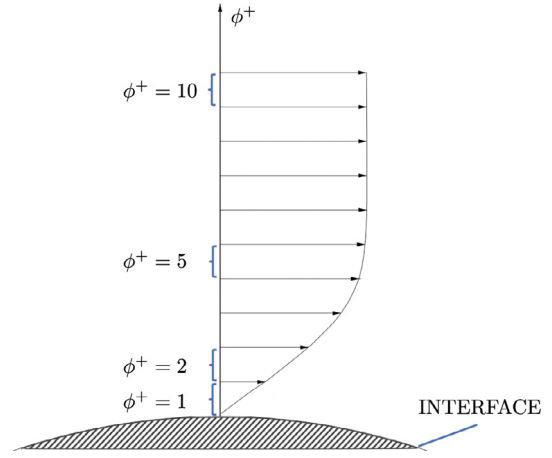


**Fig. 5.** Schematic (sizes not proportionally scaled) illustrating the layers near the droplet interface used for conditional averaging.

**Table 5**

Parameters inferred from the DNS dataset for the assessment of the interfacial boundary-layer flow structure at  $t = 2.5$ : (i)  $\hat{n}^+$  @  $\tau_{vc}^+/\tau_t^+ \approx 1$  is the distance from the interface (viscous units) at which  $\tau_{vc}^+$  and  $\tau_t^+$  are approximately equal, (ii)  $\kappa$  and (iii)  $C^+$  are the inverse of the slope and intersection constant, respectively, of the approximated log-law region curves (logarithmic scale). Abbreviation AVG indicates the average value of cases B–H.

Case	$\hat{n}^+$ @ $\tau_{vc}^+/\tau_t^+ \approx 1$	$\kappa$	$C^+$
B	10	0.41	5.8
C	9	0.40	5.1
D	8	0.41	4.6
E	12	0.42	4.4
F	11	0.41	4.7
G	8	0.42	5.9
H	9	0.38	4.8
AVG	10	0.41	5.1

the turbulent flow and droplets in terms of normalized relative velocity and fractional stresses as depicted in Figs. 8 and 9, respectively, and quantified in Table 5.

The relative velocity  $U_r^+ \equiv U^+ - U_\Sigma^+$  profiles (viscous units), spatially-averaged conditioned on the distance to the interface along interface-normal directions  $\hat{n}^+$ , are shown in Fig. 8 for cases B–H at  $t = 2.5$  and compared to the theoretical (i) linear relation  $U_r^+ = \hat{n}^+$  and (ii) logarithmic curve  $U_r^+ = (1/\kappa) \ln \hat{n}^+ + C^+$ , with  $\kappa = 0.41$  and  $C^+ = 5.1$  corresponding to the average values approximated in Table 5. Based on these results, three main observations can be extracted: (i) similar to turbulent boundary layers in wall-bounded flows, the linear relation  $U_r^+ = \hat{n}^+$  is satisfied for cases B–H in the range  $\hat{n}^+ \lesssim \mathcal{O}(1)$ ; (ii) in all cases, a log-law region of the form  $U_r^+ = (1/\kappa) \ln \hat{n}^+ + C^+$  satisfactorily approximates the relative velocity profiles for  $\hat{n}^+ \gtrsim \mathcal{O}(10)$ ; and (iii) as tabulated in Table 5, the variability of the inferred von Kármán constants  $\kappa$  and intercept coefficients  $C^+$  is small between cases, taking the average values of  $\kappa = 0.41$  and  $C^+ = 5.1$  in particular.

Profiles of the near-interface fractional contributions of the viscous  $\tau_{vc}^+ = (v_c/u_\Sigma^2) \langle du/d\hat{n} \rangle$  and Reynolds stresses  $\tau_t^+ = (-1/u_\Sigma^2) \langle u'v' \rangle$ , i.e., turbulent velocity fluctuations, to the total stress  $\tau_\Sigma^+ = \tau_{vc}^+ + \tau_t^+$  for case C (as representative of the dataset B–H) are shown in Fig. 9. The profiles depicted in the figure demarcate two clearly separated regions with a rapid transition between them. The total stresses in the first region ( $\hat{n}^+ \lesssim 10$ ) are dominated by molecular viscosity effects since  $\tau_{vc}^+ \gg \tau_t^+$ , while the second region ( $\hat{n}^+ \gtrsim 10$ ) is characterized by large Reynolds stresses, related to the appearance of significant turbulent velocity fluctuations, and resulting in  $\tau_{vc}^+ \ll \tau_t^+$ . The transition point be-

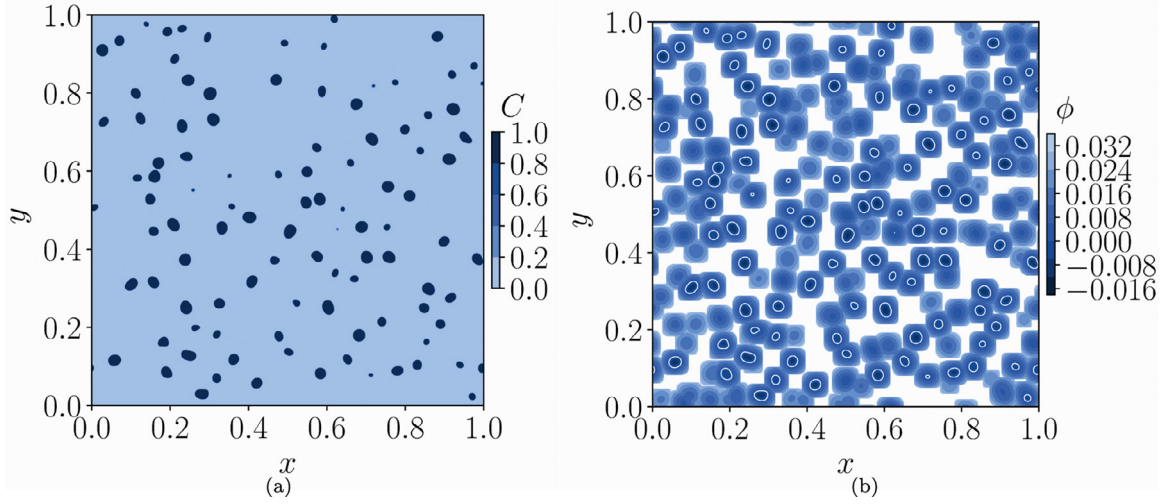


Fig. 6. Instantaneous contours in the  $x$ - $y$  plane of (a) the VoF field,  $C = C(\mathbf{x}, t)$ , and (b) the level-set field,  $\phi = \phi(\mathbf{x}, t)$ , for case C at  $t = 2.5$ .

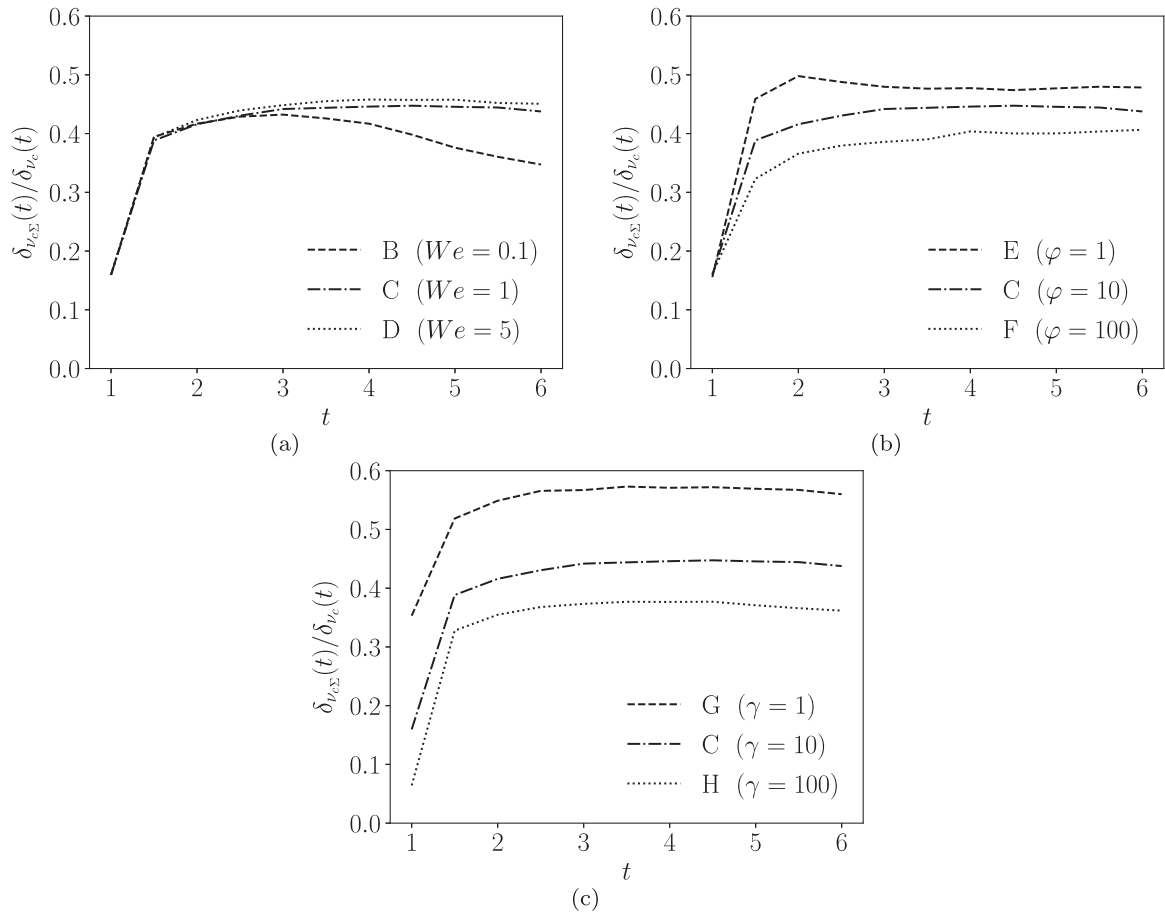
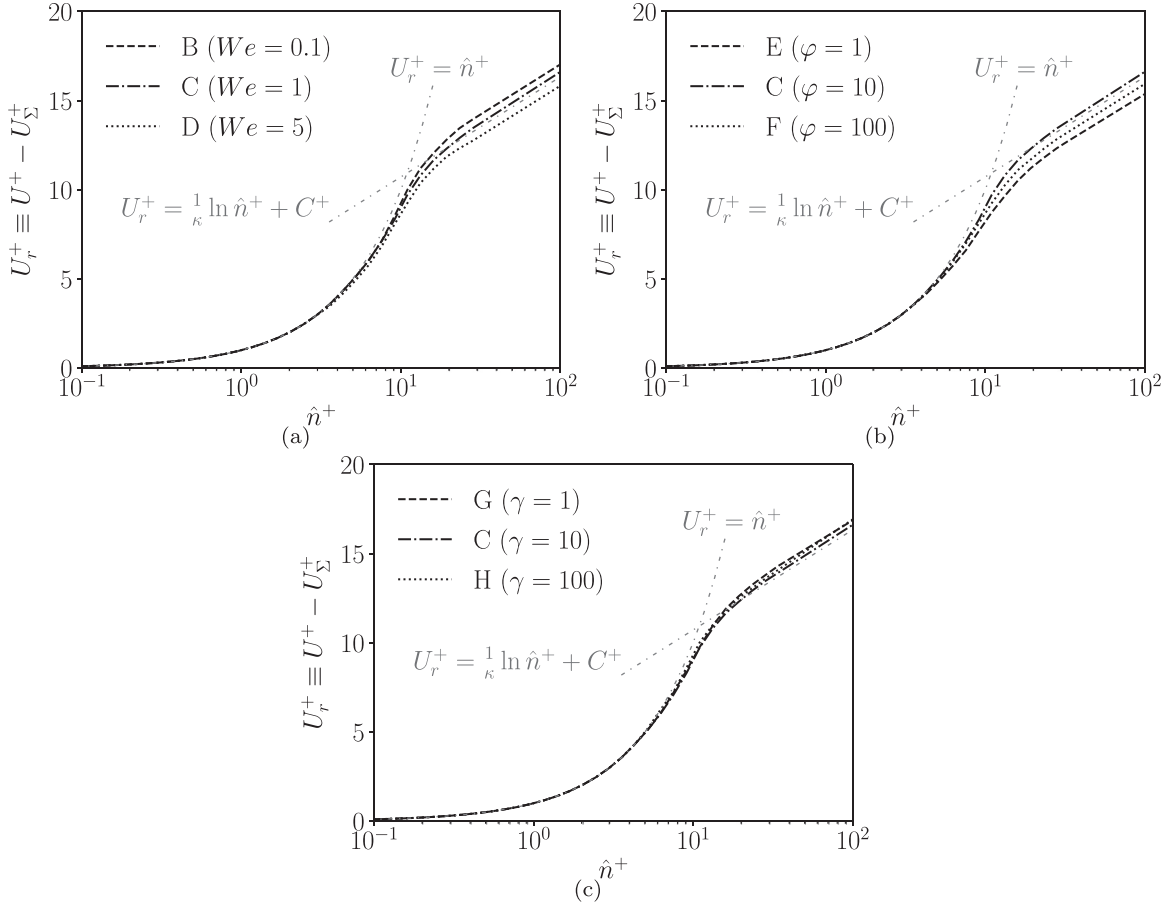


Fig. 7. Time evolution (dimensionless) of the interfacial viscous length scale in the carrier phase  $\delta_{v,\Sigma}(t)$  normalized by the mean viscous length scale of the carrier phase  $\delta_{v,c}(t)$  for varying (a) Weber number, (b) density ratio, and (c) viscosity ratio.

tween these two regions, defined as the location  $\hat{n}^+$  at which  $\tau_{v,c}^+$  and  $\tau_r^+$  are approximately equal, is found in the range  $\hat{n}^+ \approx 8$ – $12$  for cases B–H as listed in Table 5.

The analysis conducted in this section based on DNS data from cases B–H indicates therefore that, similar to the inner region of turbulent boundary layers in wall-bounded flows, the flow structure near interfaces can be separated in three distinct layers: (i) a viscous sublayer,  $\hat{n}^+ \lesssim \mathcal{O}(1)$ , where molecular viscosity dominates

over turbulent fluctuations, and characterized by a linear increase of the relative velocity with  $\hat{n}^+$  given as  $U_r^+ = \hat{n}^+$ ; (ii) a buffer layer,  $\mathcal{O}(1) \lesssim \hat{n}^+ \lesssim \mathcal{O}(10)$ , in which the momentum transport by means of molecular viscosity and turbulent fluctuations is of the same order, i.e.,  $\tau_{v,c}^+/\tau_r^+ \sim 1$ ; and (iii) a log-law region,  $\hat{n}^+ \gtrsim \mathcal{O}(10)$ , where turbulent fluctuations are the main mechanism for momentum transport, and where the relative velocity can be efficiently approximated by a logarithmic curve of the form  $U_r^+ = (1/\kappa) \ln \hat{n}^+ + C^+$ .



**Fig. 8.** Relative velocity  $U_r^+ \equiv U^+ - U_\Sigma^+$  as function of normal distance to the interface  $\hat{n}^+$  (viscous units) spatially-averaged at dimensionless time  $t = 2.5$  for varying (a) Weber number, (b) density ratio, and (c) viscosity ratio. The dashed-dotted lines correspond to the linear relation  $U_r^+ = \hat{n}^+$  and the logarithmic curve  $U_r^+ = (1/\kappa) \ln \hat{n}^+ + C^+$  with  $\kappa = 0.41$  and  $C^+ = 5.1$ .

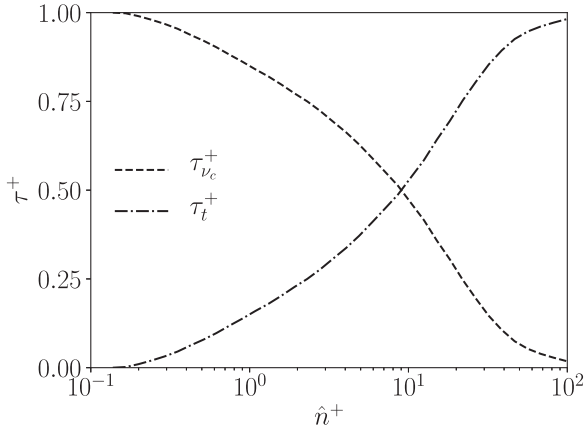


**Fig. 9.** Profiles (viscous units) of the fractional contributions of the viscous  $\tau_v^+$  and Reynolds stresses  $\tau_t^+$  to the total stress  $\tau_s^+$ . Results obtained from spatially-averaged data at dimensionless time  $t = 2.5$  for case C as representative of the dataset.

### 5.6. A priori analysis of the near-interface flow modeling approach

After analyzing the mean-velocity profile in the vicinity of interfaces by utilizing DNS data extracted from cases B-H at dimensionless time  $t = 2.5$ , the performance of the near-interface flow modeling approach proposed in Section 4 is *a priori* analyzed. For each case, the methodology followed is composed of two steps:

(1) explicitly filter the DNS velocity field, and (2) iteratively reconstruct the interface-modeled friction velocity  $u_{\tau_\Sigma}^{\text{IM}}$  by means of the algebraic closure model introduced in Eq. (22).

The details of the filtering and reconstruction steps are as follows. The filtering operation is carried out by means of a second-order Gaussian filter defined as Sagaut and Grohens (1999)

$$\bar{\phi}(\mathbf{x}) = \phi(\mathbf{x}) + \frac{\bar{\Delta}^2}{24} \frac{\partial^2 \phi}{\partial x_j^2} + \mathcal{O}(\bar{\Delta}^4), \quad (23)$$

where  $\phi$  and  $\bar{\phi}$  correspond to the velocity components of the unfiltered DNS ( $u, v, w$ ) and filtered LES ( $\bar{u}, \bar{v}, \bar{w}$ ) fields at dimensionless time  $t = 2.5$ , and the dimensionless filter width is chosen to be  $\bar{\Delta} = 1/64 \sim \ell_{\text{E1}}$ ; as a reference, the dimensionless grid resolution of the DNS dataset is  $\Delta = 1/1024$ . Next, the interface velocity  $u_\Sigma$  is approximated by the spatially-averaged LES velocities at the grid points capturing the interfaces, i.e.,  $u_\Sigma \approx \bar{u}_{\hat{n}=0}$ . Finally, the interface-modeled friction velocities  $u_{\tau_\Sigma}^{\text{IM}}$  are iteratively approximated from the algebraic model defined in Eq. (22), with  $\kappa = 0.41$  and  $C^+ = 5.1$  (average values of Table 5), at the matching locations  $\hat{n}^* u_{\tau_\Sigma}^{\text{IM}} / \nu_c = \hat{n}^+ \approx 30$ ,  $\hat{n}^* u_{\tau_\Sigma}^{\text{IM}} / \nu_c = \hat{n}^+ \approx 60$ , and  $\hat{n}^* u_{\tau_\Sigma}^{\text{IM}} / \nu_c = \hat{n}^+ \approx 90$ . The values between parenthesis correspond to the normalized relative errors with respect to  $u_{\tau_\Sigma}$  (listed in Table 3) and calculated as  $\varepsilon_{\text{rel}} \equiv 100 \times |u_{\tau_\Sigma}^{\text{IM}} - u_{\tau_\Sigma}| / u_{\tau_\Sigma}$ .

The results in terms of spatially-averaged interface velocities  $u_\Sigma$  and interface-modeled friction velocities  $u_{\tau_\Sigma}^{\text{IM}}$  at different matching locations  $\hat{n}^*$  are summarized in Table 6. Three main observations can be extracted for the set of cases B-H studied: (i) the approx-

**Table 6**

Results of the *a priori* near-interface flow modeling analysis at  $t = 2.5$  for cases B–H. The interface velocity is approximated by the spatially-averaged LES velocities at the grid points capturing the interfaces, i.e.,  $u_\Sigma \approx \bar{u}_{\hat{n}=0}$ . The interface-modeled friction velocities  $u_{\tau_\Sigma}^{\text{IM}}$  are iteratively approximated from the algebraic model defined in Eq. (22), with  $\kappa = 0.41$  and  $C^+ = 5.1$ , at the matching locations  $\hat{n}^+ u_{\tau_\Sigma}^{\text{IM}}/\nu_c = \hat{n}^+ \approx 30$  (left),  $\hat{n}^+ u_{\tau_\Sigma}^{\text{IM}}/\nu_c = \hat{n}^+ \approx 60$  (center), and  $\hat{n}^+ u_{\tau_\Sigma}^{\text{IM}}/\nu_c = \hat{n}^+ \approx 90$  (right). The values between parenthesis correspond to the normalized relative errors with respect to  $u_{\tau_\Sigma}$  (listed in Table 3) and calculated as  $\varepsilon_{\text{rel}}^{\text{IM}} \equiv 100 \times |u_{\tau_\Sigma}^{\text{IM}} - u_{\tau_\Sigma}|/u_{\tau_\Sigma}$ .

Case	$u_\Sigma$	$u_{\tau_\Sigma}^{\text{IM}} @ \hat{n}^+ \approx 30$	$u_{\tau_\Sigma}^{\text{IM}} @ \hat{n}^+ \approx 60$	$u_{\tau_\Sigma}^{\text{IM}} @ \hat{n}^+ \approx 90$
B	$2.27 \times 10^{-2}$	$1.64 \times 10^{-2}$ (4.2%)	$1.63 \times 10^{-2}$ (4.0%)	$1.63 \times 10^{-2}$ (3.8%)
C	$2.33 \times 10^{-2}$	$1.57 \times 10^{-2}$ (1.4%)	$1.57 \times 10^{-2}$ (1.4%)	$1.57 \times 10^{-2}$ (1.5%)
D	$2.68 \times 10^{-2}$	$1.48 \times 10^{-2}$ (3.0%)	$1.49 \times 10^{-2}$ (2.9%)	$1.49 \times 10^{-2}$ (2.7%)
E	$4.91 \times 10^{-2}$	$1.26 \times 10^{-2}$ (5.5%)	$1.26 \times 10^{-2}$ (5.4%)	$1.26 \times 10^{-2}$ (5.2%)
F	$1.12 \times 10^{-2}$	$1.80 \times 10^{-2}$ (2.4%)	$1.80 \times 10^{-2}$ (2.3%)	$1.80 \times 10^{-2}$ (2.2%)
G	$3.04 \times 10^{-2}$	$1.22 \times 10^{-2}$ (3.5%)	$1.22 \times 10^{-2}$ (3.2%)	$1.21 \times 10^{-2}$ (2.9%)
H	$1.91 \times 10^{-2}$	$1.89 \times 10^{-2}$ (2.5%)	$1.89 \times 10^{-2}$ (2.8%)	$1.90 \times 10^{-2}$ (3.0%)

imation of  $u_\Sigma$  as the average value of  $\bar{u}_{\hat{n}=0}$  over the grid points capturing the interfaces is an effective strategy as it provides good sensitivity to the variations particular to each simulation; (ii) for each case, the  $u_{\tau_\Sigma}^{\text{IM}}$  values do not vary significantly as a function of matching location  $\hat{n}^+$  within the log-law region; and (iii) in general, the relative reconstruction errors  $\varepsilon_{\text{rel}}^{\text{IM}}$  are (approximately) below 5%. Therefore, these results indicate that, based on *a priori* studies, the near-interface flow modeling approach proposed in this work has the potential to efficiently reduce the cost of performing LES of two-phase turbulence.

## 6. Summary, conclusions and future work

The computational cost of studying turbulence in two-phase systems can be notably reduced by means of LES approaches, in which the large eddies are resolved while their interaction with the small-scale flow motions are modeled. Away from phase interfaces, LES has proven to be (over the past decades) an attractive strategy able to reduce the simulation expense, in terms of grid points per spatial dimension  $N$ , to a linear relation with the Reynolds number given as  $N^3 \sim Re$ ; as a reference, the cost of performing DNS scales as  $N^3 \sim Re^{9/4}$ . However, analogously to the case of solid walls in single-phase turbulence, the performance of the methodology is significantly reduced due to the necessity to properly resolve with fine meshes the boundary layers generated at interfaces.

The near-interface flow modeling approach presented in this work, therefore, aims at keeping the cost of LES linear with respect to the Reynolds number when phase/fluid interfaces interact with turbulent flows. The approach is based on (i) low-pass filtering the equations of fluid motion to resolve the large scales, (ii) utilize an LES model to close the resulting filtered equations, (iii) capture with a relatively coarse grid the evolution of interfaces down to the Hinze scale, and (iv) use models similar to the ones utilized in wall-modeling of single-phase turbulence to accurately model the near-interface motions, and therefore enlarge the mesh resolution near interfaces. The first part of the methodology is to connect boundary-layer theory with the flow structure near interfaces by following Millikan's theoretical analysis applied to the case of interfaces (conceptualized as slip walls). The second part consists in proposing models, inspired from wall-modeling ideas in the present work, to represent the boundary-layer flow structure in the vicinity of interfaces.

As a first exploratory work, a straightforward model in which the interfacial-shear stress is algebraically related to the velocity as a function of distance to the interface, viz. logarithmic law applied to interfacial flow, has been chosen and *a priori* analyzed. The results obtained, based on DNS data extracted from HIT laden with finite-size droplets for different Weber numbers and ratios of carrier and dispersed phase densities and viscosities, indicate that the approach proposed has the potential to efficiently reduce, up to

several orders of magnitude depending on the ratio between Kolmogorov, Hinze and anisotropic turbulent length scales (approximately one thousand times in this work), the cost of performing LES of two-phase turbulence by modeling (instead of resolving) the viscous near-interface flow motions.

Ongoing work is focused on further assessing the performance of the modeling strategy by means of *a priori* analyses of different canonical two-phase turbulent flows and closure models in the context of HF simulations. In the mid- long-term, work will consider *a posteriori* assessments of the near-interface flow modeling in LES studies of interfacial problems, such as turbulent two-phase jets, waves and bubbly flow.

## Declaration of Competing Interest

The authors declare that they have no known competing financial interests or personal relationships that could have appeared to influence the work reported in this paper.

## CRediT authorship contribution statement

**Luís Jofre:** Conceptualization, Formal analysis, Funding acquisition, Investigation, Software, Writing - original draft. **Michael S. Dodd:** Conceptualization, Formal analysis, Investigation, Software, Writing - original draft. **Joan Grau:** Formal analysis, Investigation, Software. **Ricardo Torres:** Formal analysis, Investigation, Writing - review & editing.

## Acknowledgments

This research was financially supported by the Beatriz Galindo Program (Distinguished Researcher, BGP18/00026) of the Ministerio de Ciencia, Innovación y Universidades, Spain. The authors thank the anonymous reviewers for their valuable comments and suggestions that helped improve the quality of the paper.

The work presented in this paper used the Extreme Science and Engineering Discovery Environment (XSEDE), which is supported by the National Science Foundation (NSF), Grant No. ACI-1548562. In particular, the authors acknowledge the Texas Advanced Computing Center (TACC) at The University of Texas at Austin through allocation TG-CTS190073 for providing high-performance computing resources that have contributed to the research presented in this paper.

## References

- Agbaglah, G., Chiodi, R., Desjardins, O., 2017. Numerical simulation of the initial destabilization of an air-blasted liquid layer. *J. Fluid Mech.* 812, 1024–1038.
- Almagro, A., García-Villalba, M., Flores, O., 2017. A numerical study of a variable-density low-speed turbulent mixing layer. *J. Fluid Mech.* 830, 569–601.
- Aniszewski, W., Boguslawski, A., Marek, M., Tyliczszak, A., 2012. A new approach to sub-grid surface tension for LES of two-phase flows. *J. Comput. Phys.* 231, 7368–7397.

- Balcázar, N., Lehmkuhl, O., Jofre, L., Oliva, A., 2015. Level-set simulations of buoyancy-driven motion of single and multiple bubbles. *Int. J. Heat Fluid Flow* 56, 91–107.
- Baraldi, A., Dodd, M.S., Ferrante, A., 2014. A mass-conserving volume-of-fluid method: volume tracking and droplet surface-tension in incompressible isotropic turbulence. *Comput. Fluids* 96, 322–337.
- Bose, S.T., Park, G.I., 2018. Wall-modeled large-eddy simulation for complex turbulent flows. *Annu. Rev. Fluid Mech.* 50, 535–561.
- Capecelatro, J., Desjardins, O., 2013. An Euler-Lagrange strategy for simulating particle-laden flows. *J. Comput. Phys.* 238, 1–31.
- Chan, W.H.R., Mirjalili, S., Jain, S.S., Urzay, J., Mani, A., Moin, P., 2019. Birth of microbubbles in turbulent breaking waves. *Phys. Rev. Fluids* 4, 100508.
- Crowe, C.T., Trout, T.R., Chung, J.N., 1996. Numerical models for two-phase turbulent flows. *Annu. Rev. Fluid Mech.* 28, 11–43.
- Csanady, G.T., 1997. The “slip wall” of the free surface. *J. Oceanogr.* 53, 67–80.
- Deardorff, J.W., 1970. A numerical study of three-dimensional turbulent channel flow at large Reynolds numbers. *J. Fluid Mech.* 41, 453–480.
- Deen, N.G., Solberg, T., Hjertager, B.H., 2001. Large eddy simulation of the gas-liquid fluid flow in a square cross-sectioned bubble column. *Chem. Eng. Sci.* 56, 6341–6349.
- Deike, L., Melville, W.K., Popinet, S., 2016. Air entrainment and bubble statistics in breaking waves. *J. Fluid Mech.* 801, 91–129.
- Desjardins, O., Pitsch, H., 2010. Detailed numerical investigation of turbulent atomization of liquid jets. *Atom. Spray.* 20, 311–336.
- Dodd, M.S., Ferrante, A., 2014. A fast pressure-correction method for incompressible two-fluid flows. *J. Comput. Phys.* 273, 416–434.
- Dodd, M.S., Ferrante, A., 2016. On the interaction of Taylor length scale size droplets and isotropic turbulence. *J. Fluid Mech.* 806, 356–412.
- Dodd, M.S., Jofre, L., 2018. Tensor-based analysis of the flow topology in droplet-laden homogeneous isotropic turbulence. *Annu. Res. Briefs, Cent. Turbul. Res.* 35–45.
- Dodd, M.S., Jofre, L., 2019. Small-scale flow topologies in decaying isotropic turbulence laden with finite-size droplets. *Phys. Rev. Fluids* 4, 064303.
- Domino, S.P., Jofre, L., Iaccarino, G., 2019. The suitability of hybrid meshes for low-Mach large-eddy simulation. In: *Proceedings of the Seventeenth Biennial Summer Program, Center for Turbulence Research, Stanford University*, pp. 97–106.
- Elghobashi, S., 2019. Direct numerical simulation of turbulent flows laden with droplets or bubbles. *Annu. Rev. Fluid Mech.* 51, 217–244.
- Faeth, G.M., Hsiang, L.-P., Wu, P.-K., 1995. Structure and breakup properties of sprays. *Int. J. Multiph. Flow* 51, 217–244.
- Gorokhovskii, M., Herrmann, M., 2008. Modeling primary atomization. *Annu. Rev. Fluid Mech.* 40, 343–366.
- Grabowski, W.W., Wang, L.-P., 2013. Growth of cloud droplets in a turbulent environment. *Annu. Rev. Fluid Mech.* 45, 293–324.
- Hasslberger, J., Ketterl, S., Klein, M., 2020. A-priori assessment of interfacial sub-grid scale closures in the two-phase flow LES context. *Flow Turbul. Combust.* doi:10.1007/s10494-020-00114-4.
- Herrmann, M., 2013. A sub-grid surface dynamics model for sub-filter surface tension induced interface dynamics. *Comput. Fluids* 87, 92–101.
- Hinze, J.O., 1955. Fundamentals of the hydrodynamic mechanism of slitting in dispersion processes. *AIChE J.* 1, 289–295.
- Jofre, L., Borrell, R., Lehmkuhl, O., Oliva, A., 2015. Parallel load balancing strategy for Volume-of-Fluid methods on 3-D unstructured meshes. *J. Comput. Phys.* 282, 269–288.
- Jofre, L., Domino, S.P., Iaccarino, G., 2018. A framework for characterizing structural uncertainty in large-eddy simulation closures. *Flow Turbul. Combust.* 100 (2), 341–363.
- Jofre, L., Domino, S.P., Iaccarino, G., 2019. Eigensensitivity analysis of subgrid-scale stresses in large-eddy simulation of a turbulent axisymmetric jet. *Int. J. Heat Fluid Flow* 77, 314–335.
- Jofre, L., Lehmkuhl, O., Castro, J., Oliva, A., 2010. A PLIC-VOF implementation on parallel 3D unstructured meshes. *Proceedings of the Fifth ECCOMAS CFD*, 1–15.
- Jofre, L., Lehmkuhl, O., Castro, J., Oliva, A., 2014. A 3-D Volume-of-Fluid advection method based on cell-vertex velocities for unstructured meshes. *Comput. Fluids* 94, 14–29.
- Jofre, L., del Rosario, Z.R., Iaccarino, G., 2020. Data-driven dimensional analysis of heat transfer in irradiated particle-laden turbulent flow. *Int. J. Multiph. Flow* 125, 103198.
- Jofre, L., Urzay, J., 2017. Interface dynamics in the transcritical flow of liquid fuels into high-pressure combustors. In: *Proceedings of the 53rd AIAA/SAE/ASEE Joint Propulsion Conference, Paper #2017-4040*.
- Kaario, O., Vuorinen, V., Hulkkonen, T., Keskinen, K., Nuutinen, M., Larmi, M., Tanner, F.X., 2013. Large eddy simulation of high gas density effects in fuel sprays. *Atom. Spray.* 23, 297–325.
- Kawai, S., Larsson, J., 2012. Wall-modeling in large eddy simulation: length scales, grid resolution, and accuracy. *Phys. Fluids* 24, 015105.
- Klein, M., Ketterl, S., Engelmann, L., Kempf, A., Kobayashi, H., 2020. Regularized, parameter free scale similarity type models for large eddy simulation. *Int. J. Heat Fluid Flow* 81, 108496.
- Klein, M., Ketterl, S., Hasslberger, J., 2019. Large eddy simulation of multiphase flows using the volume of fluid method: Part 1 – Governing equations and a-priori analysis. *Exp. Comput. Multiph. Flow* 1, 130–144.
- Kolmogorov, A., 1949. On the breakage of drops in a turbulent flow. *Dokl. Akad. Navk. SSSR* 66, 825–828.
- Kolmogorov, A.N., 1941. The local structure of turbulence in incompressible viscous fluid for very large Reynolds numbers. *Dokl. Akad. Nauk SSSR* 30, 299–303.
- Labourasse, E., Lacanette, D., Toutant, A., Lubin, P., Vincent, S., Lebaigue, O., Caltagirone, J.-P., Sagaut, P., 2007. Towards large eddy simulation of isothermal two-phase flows: governing equations and a priori tests. *Int. J. Multiph. Flow* 33, 1–39.
- Lakehal, D., 2010. LEIS for the prediction of turbulent multifluid flows applied to thermal-hydraulics applications. *Nucl. Eng. Des.* 240, 2096–2106.
- Lakehal, D., 2017. Large-eddy simulation of convective wall-boiling flow along an idealized PWR rod bundle. *Nucl. Eng. Des.* 321, 104–117.
- Lakehal, D., 2018. Status and future developments of large-eddy simulation of turbulent multi-fluid flows (LEIS and LESS). *Int. J. Multiph. Flow* 104, 322–337.
- Lakehal, D., Liovic, P., 2011. Turbulent structure and interaction with steep breaking waves. *J. Fluid Mech.* 674, 522–577.
- Lakehal, D., Smith, B., Milelli, M., 2002. Large-eddy simulation of bubbly turbulent shear flows. *J. Turbul.* 3, 1–22.
- Leonard, A., 1974. Energy cascade in large-eddy simulations of turbulent fluid flows. *Adv. Geophys.* A 18, 237–248.
- Lesieur, M., Metais, O., 1996. New trends in large-eddy simulations of turbulence. *Annu. Rev. Fluid Mech.* 28, 45–82.
- Lewiner, T., Lopes, H., Vieira, A.W., Tavares, G., 2003. Efficient implementation of Marching Cubes’ cases with topological guarantees. *J. Graph. Tools* 8, 1–15.
- Lin, S., Lu, J., Tryggvason, G., Zhang, Y., 2018. A numerical study of oscillation induced coalescence in bubbly flows. *Phys. Fluids* 30, 127105.
- Ling, Y., Fuster, D., Tryggvason, G., Zaleski, S., 2019. A two-phase mixing layer between parallel gas and liquid streams: multiphase turbulence statistics and influence of interfacial instability. *J. Fluid Mech.* 859, 268–307.
- Lu, J., Muradoglu, M., Tryggvason, G., 2017. Effect of insoluble surfactant on turbulent bubbly flows in vertical channels. *Int. J. Multiph. Flow* 95, 135–143.
- Lucci, F., Ferrante, A., Elghobashi, S., 2010. Modulation of isotropic turbulence by particles of Taylor length-scale size. *J. Fluid Mech.* 650, 5–55.
- Lund, T.S., 2003. The use of explicit filters in large eddy simulation. *Comput. Math. Appl.* 46, 603–616.
- Marsden, A.L., Vasilyev, O.V., Moin, P., 2002. Construction of commutative filters for LES on unstructured meshes. *J. Comput. Phys.* 175, 584–603.
- Martínez-Bazán, C., Montañés, J.L., Lasheras, J.C., 1999. On the breakup of an air bubble injected into a fully developed turbulent flow. Part 1. Breakup frequency. *J. Fluid Mech.* 401, 157–182.
- Masquelet, M., Yan, J., Dord, A., Laskowski, G., Shunn, L., Jofre, L., Iaccarino, G., 2017. Uncertainty quantification in large eddy simulations of a rich-dome aviation gas turbine. In: *Proceedings of the ASME Turbo Expo 2017, GT2017-64835*, pp. 1–11.
- Meneveau, C., Katz, J., 2000. Scale-invariance and turbulence models for large-eddy simulation. *Annu. Rev. Fluid Mech.* 32, 1–32.
- Millikan, C.B., 1939. A critical discussion of turbulent flows in channels and circular tubes. In: *Proceedings of the Fifth International Congress on Applied Mechanics (Cambridge, MA)*, pp. 386–392.
- Mittal, R., Iaccarino, G., 2005. Immersed boundary methods. *Annu. Rev. Fluid Mech.* 37, 239–261.
- Moin, P., Mahesh, K., 1998. Direct numerical simulation: a tool in turbulence research. *Annu. Rev. Fluid Mech.* 30, 539–578.
- Pilch, M., Erdmann, C.A., 1987. Use of breakup time data and velocity history data to predict the maximum size of stable fragments. *Int. J. Multiph. Flow* 13, 741–757.
- Piomelli, U., Balaras, E., 2002. Wall-layer models for large-eddy simulations. *Annu. Rev. Fluid Mech.* 34, 349–374.
- Pope, S.B., 2000. *Turbulent Flows*. Cambridge University Press.
- Prosperetti, A., 2017. Vapor bubbles. *Annu. Rev. Fluid Mech.* 49, 221–248.
- Rasthofer, U., Wermelinger, F., Karnakov, P., Šukys, J., Koumoutsakos, P., 2019. Computational study of the collapse of a cloud with 12500 gas bubbles in a liquid. *Phys. Rev. Fluids* 4, 063602.
- Richardson, L.F., 1922. *Weather Prediction by Numerical Process*. Cambridge University Press.
- Rodríguez-Rodríguez, J., Sevilla, A., Martínez-Bazán, C., Gordillo, J.M., 2015. Generation of microbubbles with applications to industry and medicine. *Annu. Rev. Fluid Mech.* 47, 405–429.
- Rogallo, R.S., Moin, P., 1984. Numerical simulation of turbulent flows. *Annu. Rev. Fluid Mech.* 16, 99–137.
- Saeedipour, M., Schneiderbauer, S., 2019. A new approach to include surface tension in the subgrid eddy viscosity for the two-phase LES. *Int. J. Multiph. Flow* 121, 103128.
- Saeedipour, M., Vincent, S., Pirker, S., 2019. Large eddy simulation of turbulent interfacial flows using approximate deconvolution model. *Int. J. Multiph. Flow* 112, 286–299.
- Sagaut, P., Germano, M., 2005. On the filtering paradigm for LES of flows with discontinuities. *J. Turbul.* 6, N23.
- Sagaut, P., Grohens, R., 1999. Discrete filters for large eddy simulation. *Int. J. Numer. Methods Fluids* 31, 1195–1220.
- Schlichting, H., Gersten, K., 2016. *Boundary-Layer Theory*. Springer.
- Schumann, U., 1977. Realizability of Reynolds-stress turbulence models. *Phys. Fluids* 20, 721.
- Shinjo, J., Umemura, A., 2010. Simulation of liquid jet primary breakup: dynamics of ligaments and droplet formation. *Int. J. Multiph. Flow* 36, 513–532.
- Sirignano, W., 2002. Volume averaging for the analysis of turbulent spray flows. *Int. J. Multiph. Flow* 31, 675–705.
- Sirignano, W.A., 1983. Fuel droplet vaporization and spray combustion theory. *Prog. Energy Combust. Sci.* 9, 291–322.
- Soligo, G., Roccon, A., Soldati, A., 2019. Breakage, coalescence and size distribution of surfactant-laden droplets in turbulent flow. *J. Fluid Mech.* 881, 244–282.

- Toutant, A., Chandesris, M., Jamet, D., Lebaigue, O., 2009. Jump conditions for filtered quantities at an under-resolved discontinuous interface. *Int. J. Multiph. Flow* 35, 1100–1118.
- Tryggvason, G., Dabiri, S., Aboulhasanzadeh, B., Lu, J., 2013. Multiscale considerations in direct numerical simulations of multiphase flows. *Phys. Fluids* 25, 031302.
- Tryggvason, G., Scardovelli, R., Zaleski, S., 2011. *Direct Numerical Simulations of Gas-Liquid Multiphase Flows*. Cambridge University Press.
- Valle, N., Trias, F.X., Castro, J., 2020. An energy-preserving level set method for multiphase flows. *J. Comput. Phys.* 400, 108991.
- Vasilyev, O.V., Lund, T.S., Moin, P., 1998. A general class of commutative filters for LES in complex geometries. *J. Comput. Phys.* 146, 82–104.
- Yang, D., Chen, B., Socolofsky, S.A., Chamecki, M., Meneveau, C., 2016. Large-eddy simulation and parameterization of buoyant plume dynamics in stratified flow. *J. Fluid Mech.* 794, 798–833.